ELSEVIER

Nuclear Instruments and Methods in Physics Research B 183 (2001) 48–61

NIM B
Beam Interactions with Materials & Atoms

www.elsevier.com/locate/nimb

High-resolution elastic recoil detection utilizing Bayesian probability theory

P. Neumaier [a,*], G. Dollinger [a], A. Bergmaier [a], I. Genchev [a], L. Görgens [a], R. Fischer [b], C. Ronning [c], H. Hofsäss [c]

[a] *Technische Universität München, Physik Department E12, James-Franck-Str., D-85748 Garching, Germany*
[b] *Centre for Interdisciplinary Plasma Science, Max-Planck-Institut für Plasmaphysik, EURATOM Association, D-85748 Garching, Germany*
[c] *Universität Göttingen, II. Physikalisches Institut, Bunsenstr. 7-9, D-37073 Göttingen, Germany*

Received 21 November 2000; received in revised form 28 December 2000

Abstract

Elastic recoil detection (ERD) analysis is improved in view of depth resolution and the reliability of the measured spectra. Good statistics at even low ion fluences is obtained utilizing a large solid angle of 5 msr at the Munich Q3D magnetic spectrograph and using a 40 MeV ^{197}Au beam. In this way the elemental depth profiles are not essentially altered during analysis even if distributions with area densities below 1×10^{14} atoms/cm^2 are measured. As the energy spread due to the angular acceptance is fully eliminated by ion-optical and numerical corrections, an accurate and reliable apparatus function is derived. It allows to deconvolute the measured spectra using the adaptive kernel method, a maximum entropy concept in the framework of Bayesian probability theory. In addition, the uncertainty of the reconstructed spectra is quantified. The concepts are demonstrated at ^{13}C depth profiles measured at ultra-thin films of tetrahedral amorphous carbon (ta-C). Depth scales of those profiles are given with an accuracy of 1.4×10^{15} atoms/cm^2.

PACS: 81.70.Yp; 68.55.Ln
Keywords: High-resolution depth profiling; Elastic recoil detection; Bayesian data analysis; Tetrahedral amorphous carbon

1. Introduction

High-resolution elastic recoil detection (ERD) analysis gives the opportunity to resolve even single monolayers if heavy ion beams with energies of about 0.5 *A* MeV (e.g. 60 MeV ^{127}I) are utilized [1]. However, two problems occur when optimum depth resolution is strived for ERD analysis.

The first one is irradiation damage which is a general limit for any ion-beam analysis technique. It becomes most significant, if ultra-thin layers or small fractions of an atomic layer (e.g. less than

* Corresponding author. Tel.: +49-0-89-289-14286; fax: +49-0-89-289-12297.
E-mail address: peter.neumaier@physik.tu-muenchen.de (P. Neumaier).

0168-583X/01/$ - see front matter
PII: S0168-583X(01)00347-0

10^{15} atoms/cm^2) are analyzed. The damage effect of interest in view of sensitivity and depth resolution is the change of the original depth profiles. The profiles should not be altered until the desired measurements have been performed. Especially the analysis of light elements (e.g. H, N, O), being a main subject of ERD analysis, is often more critical than analysis of heavier ones since light elements can be mobile if once activated by any ion-beam stimulated process. Thus, the ratio of detection cross-section to damage cross-section has to be maximized in order to keep irradiation damage as small as possible. This can be done using a large solid angle of detection and reducing the energy per nucleus of the utilized ion beam [2].

The second severe problem using ERD for depth profiling is that depth resolution decreases with increasing depth due to energy-loss straggling and small-angle scattering effects [1]. In order to improve depth resolution in larger depths and to calculate the accuracy of deduced elemental profiles, the measured spectra have to be deconvoluted with respect to an apparatus function which contains all effects of ion-beam and detector induced energy spreads as well as energy-loss straggling and small-angle scattering effects. In doing so the reliability of the deconvoluted spectra strongly depends on the accuracy of determining this apparatus function.

The paper will deal with both: how to get a stable and reliable high-resolution detector response at large solid angles of detection utilizing heavy ion beams with energies of about 0.2 A MeV and how to achieve an accurate and reliable deconvolution of the measured spectra. First, ERD analysis using a Q3D magnetic spectrograph in combination with a new focal-plane detector will be presented (Section 2). After presenting the adaptive kernel method, a deconvolution procedure in the framework of Bayesian probability theory, the determination of an accurate apparatus function for the deconvolution of measured ERD spectra is introduced in Section 3. The potential of the method will be demonstrated in Section 4 showing the analysis of ultra-thin films of tetrahedral amorphous carbon (ta-C).

2. Elastic recoil detection (ERD) using a magnetic spectrograph

The experimental arrangement for ERD measurements with high depth resolution is shown in Fig. 1. Ion beams of 20 MeV ^{35}Cl, 25 MeV ^{35}Cl and, in order to reduce irradiation damage effects, of 40 MeV ^{197}Au were used. The ions hit the samples at incident angles of 4° to 7.5° relative to the surface while the scattering angle was always 15°. The recoil ions were detected using the Munich Q3D magnetic spectrograph [3].

2.1. Correction of the kinematic shift

As mentioned above, large solid angles of detection $\Delta\Omega$ are required when quantitative analysis of small elemental amounts is desired. But the strong kinematic energy shift $\Delta E(\varphi, \Delta\varphi)$ due to a variation $\Delta\varphi$ in scattering angle φ usually limits the solid angle of detection $\Delta\Omega$ when high energy resolution is required [4]. The kinematic shift for an angle variation $\Delta\varphi$ can be expanded in a Taylor series,

$$\frac{\Delta E}{E} = -2 \cdot \tan\varphi \cdot \Delta\varphi + (\tan^2\varphi - 1) \cdot \Delta\varphi^2 + \frac{4}{3} \cdot \tan\varphi \cdot \Delta\varphi^3 + \cdots. \quad (1)$$

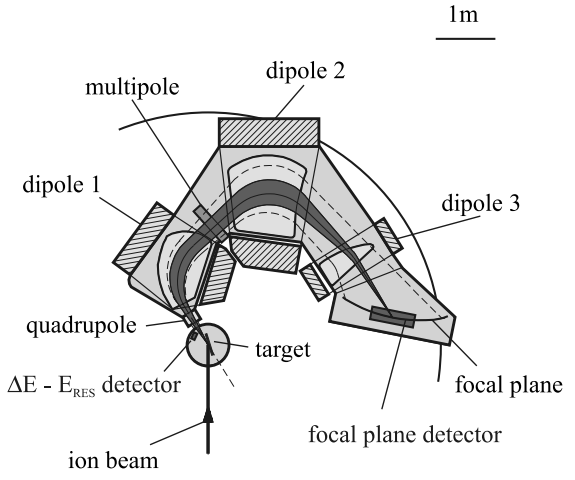

Fig. 1. Experimental arrangement for high-resolution depth profiling.

Thus, a variation of scattering angle $\varphi = 15°$ by $\Delta\varphi = \pm 3.2°$, which mainly are the conditions used at the Q3D, results in a negative first-order energy shift $\Delta E/E$ of about 6%. The first-order effect which dominates the kinematic shift even at those small scattering angles can be reduced by further reducing the scattering angle. However, at scattering angles being realistic for ERD experiments, e.g. not suffering too much from surface roughness or bending and from lateral spread at small incident angles, the kinematic shift has to be corrected for, if a relative energy resolution of about 5×10^{-4} is desired. The multipole element of the Q3D magnetic spectrograph is an ion-optical element, which is used to correct for the kinematic shift up to the third order [3]. This correction is done on-line by adjusting the multipoles of the magnetic spectrograph in order to minimize the difference of the angle-position correlation from a vertical line. The procedure is described in detail in [4] and requires information on the scattering angle for each event. In earlier experiments the angular information was obtained by two independent position measurements using two proportional counters positioned near the focal plane of the Q3D magnetic spectrograph with a distance of 6 cm apart from each other [5]. The originally achieved angular resolution of about 35 mrad implicates two disadvantages: at first it limits the accuracy of the on-line correction by adjusting the multipoles and, secondly, a numerical off-line correction is prevented, because the poor angular resolution would be transferred into a poor energy resolution. An additional problem arises due to the aspired minimization of irradiation damage requiring ion-beam energies of 0.1 A MeV to 0.3 A MeV, which is much less than used in previous experiments [2]. Especially for light recoil ions this implicates an increasing angular spread in the entrance foil of the proportional counters and, therefore, a further decrease of the angular resolution. To overcome these limitations, another concept for the focal-plane detector is introduced.

2.2. A new focal-plane detector

The new focal plane detector [6] consists of a single-wire proportional counter and a solid-state detector array (Fig. 2). The position-sensitive proportional counter contains a resistive wire which divides the detected charge to both sides. The position is determined by the ratio of the difference of the detected signal height at each side and its sum. A position resolution better than 3.5 mm was achieved for the 1.5 m long detector [6]. From the sum of the signals detected in the proportional counter specific energy losses of the detected recoil ions are obtained. Having passed the proportional counter the recoiled ions are stopped within the 1.4 m long solid-state detector consisting of 128 silicon PIN diodes (11×11 mm^2 each, 10×10 mm^2 active), where a residual energy and a timing signal are generated. The residual energy measured in the diodes and the measured energy loss in the proportional counter provide the total energy of the recoils. The nuclear charge of the detected recoil ions is determined using the ΔE signal and the total energy as it is done for conventional ERD [7]. The mass of the recoil ions is identified using the total energy and the momentum-over-charge ratio determined by the position in the focal plane. Therefore, the detected particles can be fully identified and depth profiles of each isotope can, in principle, be calculated [5].

According to the experiment's geometry (Fig. 1) a larger scattering angle and, therefore, smaller recoil energy is related to a longer flight path of the detected ions and vice versa. For this reason the scattering angle is revealed by a time-of-flight (TOF) measurement, which allows an increased angular resolution [8]. To get a TOF signal a

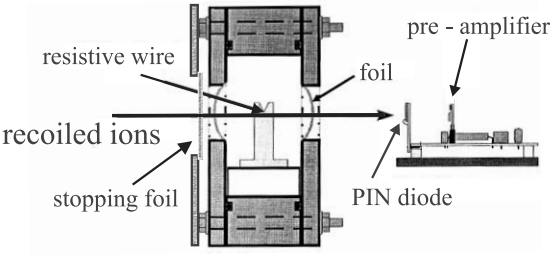

Fig. 2. Cross-section of the focal-plane detector of the Q3D. It consists of a proportional counter and solid-state detector array. If necessary, an additional stopping foil is used to prevent the penetration of the proportional counter by selected particles, e.g. backscattered beam ions.

pulsed beam is used which is generated by a buncher system at the low-energy side of the Munich tandem accelerator and a chopper at the high-energy side. The time width of the beam is about 1 ns at the target chamber of the Q3D. The starting events are drawn from the timing signals of the PIN diodes of the focal-plane detector while the corresponding stopping events are created from the RF system driving the buncher and chopper. Fig. 3(a) shows the TOF-position spectrum of $^{12}C^{5+}$ ions recoiled off a 5 μg/cm^2 thick carbon foil, perpendicularly penetrated by 20 MeV ^{35}Cl ions. It exhibits the same position in the focal plane for all measured TOF signals (and therewith all accepted scattering angles) and, therefore, represents an optimum on-line correction by adjusting the multipoles of the Q3D magnetic spectrograph. The projection towards the time axis (Fig. 3(b)) reveals an overall timing resolution of about 3 ns. It corresponds to an angular resolution of about 4 mrad at an angular acceptance of 110 mrad. Thus, the angular resolution has been improved by one order of magnitude compared to that obtained using the old focal-plane detector.

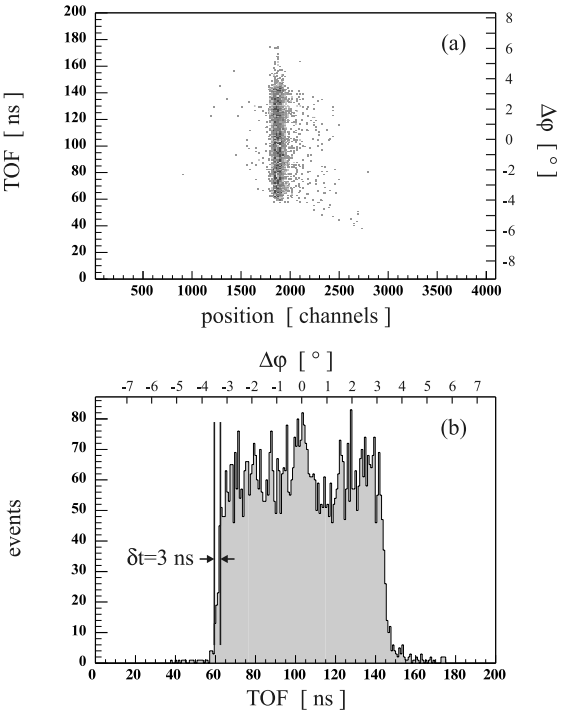

Fig. 3. (a) TOF-position spectrum of $^{12}C^{5+}$ ions recoiled of a 5 μg/cm^2 thick carbon foil, perpendicularly penetrated by 20 MeV ^{35}Cl ions. The projection towards the time axis (b) reveals an overall timing resolution $\delta t \approx 3$ ns, which corresponds to an angular resolution $\delta\varphi \approx 4$ mrad.

2.3. Correction of geometrical effects

Besides the kinematic effect discussed in the previous section, with increasing depth an additional effect influences the energy of recoils scattered to different angles. It is often called a geometric effect because it arises due to path-length differences of the scattered ions detected at different angles [9]. These path-length differences induce a rotation in the angle-energy spectra, which is opposite to the rotation caused by kinematic effects. The ion-optical performance of the Q3D gives the possibility to correct for the sum of both effects by optimization of the incident angle [4]. The angular resolution of about 4 mrad enables an additional correction using a software procedure. Slopes of ±80 mrad per 1% of relative energy loss in angle versus energy spectra can be numerically corrected for providing a relative energy resolution better than 5×10^{-4}. The result of both corrections is shown in Fig. 4. It exhibits the corrected angle-energy spectrum of $^{13}C^{5+}$ recoil ions of a $^{13}C/^{12}C$ multilayer sample, when 25 MeV ^{35}Cl ions impinge at an angle of 7.5° to the surface and a scattering angle of 15° is used. The projection of the spectrum in Fig. 4 to the energy axis and the conversion of the energy scale to a depth scale using the effective stopping powers of the impinging and recoiled ions reveals the high-resolution depth profile [5].

The introduced method of angular correction is good enough to fully correct for all the energy shifts induced by the large solid angle of detection. As the described performance holds even for recoil energies of a few MeV, projectile energies of 0.1 A MeV to 0.5 A MeV can be utilized. This guarantees good statistics with low ion fluences and small irradiation damage, because the scattering cross-section scales as A^2/E^2, whereas the total cross-section for the displacement of an atom due to nuclear collisions scales as A/E for high energies [10]. Lowering beam energy per nucleus makes a

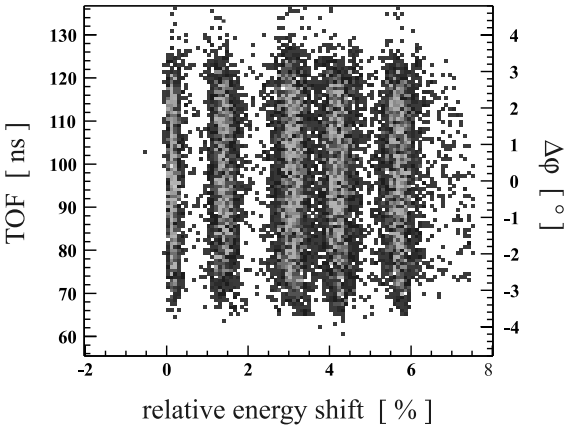

Fig. 4. Angle-energy spectrum of $^{13}C^{5+}$ ions recoiled of a $^{13}C/^{12}C$ multilayer sample measured with the focal-plane detector. An optimum incident angle of 7.5° is used, path-length differences and the kinematic shift compensate each other in first-order. Remaining small angle-position dependences are corrected with suitable software.

smaller beam damage. This improvement in view of irradiation damage is even much stronger, if the sample suffers from irradiation damage introduced by electronic processes such as thermal spike [11,12] or Coulomb explosion [13] phenomena, since electronic stopping power for heavy ions decreases at those energies below the stopping-power maximum.

However, as a drawback, depth resolution suffers from reduced beam energies, especially at large depths, due to the increasing relative energy spread and increasing small-angle scattering effects [1]. Therefore, a reduction of beam energy much lower than e.g. 0.1 A MeV is not strived for.

3. Bayesian data analysis

In ERD analysis the depth resolution essentially depends on the relative energy resolution $\Delta E/E$ of the total ERD apparatus. Beside broadening effects induced by specific sample properties as inhomogeneity and surface roughness the energy resolution is generally limited by the relative energy spread of the beam, a kinematical broadening due to beam divergence, the intrinsic detector resolution, broadening effects due to angular acceptance, the energy spread due to the thermal motion of the analyzed atoms (Doppler effect), and the depth-dependent energy spread introduced by energy-loss straggling and also multiple scattering [10].

As described in the previous section, the energy spread due to angular acceptance is negligible in our case. All contributions to energy broadening add to a transfer function of the whole system, which is called the apparatus function $A(E', E - E')$. The broadened spectrum $\tilde{f}(E)$ is given by

$$\tilde{f}(E) = \int_{-\infty}^{\infty} f(E')A(E', E - E')\,\mathrm{d}E', \tag{2}$$

where $f(E)$ is the spectrum that would be measured for an ideal system with no energy broadening. Due to the dependence on E' of the apparatus function A, Eq. (2) is not strictly a convolution, though it will be denoted as convolution in the following. The determination of the deconvoluted spectrum $f(E)$ from the measured spectrum $\tilde{f}(E)$, taking into account the apparatus function $A(E', E - E')$ and its errors as well as the errors of the measured spectrum $\tilde{f}(E)$, is not trivial at all. A consistent probability theory to obtain unbiased results from noisy experimental data is provided by Bayesian probability theory.

3.1. Bayesian probability theory

The direct inversion of Eq. (2) is ill-posed, if the eigenvalue spectrum of the apparatus function $A(E', E - E')$ varies over orders of magnitude as it is the normal case. It leads to meaningless results, since the statistical error of the experimental data is amplified by the inverse of the small eigenvalues. A self-consistent mathematical tool, which takes into account the statistical nature of the error properly, is given by the Bayesian probability theory, which allows to exploit any type of testable information, such as noisy experimental data, expectation values and other forms of prior knowledge [14]. An important class of problems comprises the determination of positive and additive distribution (PAD) functions, such as the ERD spectra. The Bayesian probability theory combined with the entropic prior is referred to as

quantified maximum entropy (QME) and has been applied successfully to various data analysis problems [15,16]. The QME procedure and a recently developed extension of QME, the adaptive kernel method, are described in [14], the mathematical and numerical details of QME are explained in [17]. Here, we will merely outline the key idea.

The goal is to determine the posterior probability density $P(f \mid d,\sigma,A,I)$ for the intrinsic discrete ERD spectrum f with f_j events at the N energies E_j, respectively, given N_d experimental data d_i, the respective errors σ_i, the apparatus function (A_{ij}) and further prior knowledge summarized in I. The vertical bar in the notation denotes a conditional property, based on either empirical or theoretical information. The posterior probability density represents all the information necessary to decide how reasonable a reconstruction f is. It reveals many quantities of interest, such as the most probable solution $\hat{f} = \max_f P(f \mid d,I)$, the mean $\langle f_j\rangle = \int f_j P(f \mid d,I)\mathrm{d}^N f$, and confidence intervals via the variance $\mathrm{var}(f_j) = \langle f_j^2\rangle - \langle f_j\rangle^2$. Bayes theorem is a consequence of the two forms of the product rule $P(X,Y \mid Z) = P(X \mid Y,Z)\times\ P(Y \mid Z) = P(Y \mid X,Z)P(X \mid Z)$, where X, Y and Z are propositions. It relates the yet unknown $P(f \mid d,\sigma,A,I)$ to quantities that are known, namely the likelihood probability density $P(d \mid f,\sigma,A,I)$ and the prior probability density $P(f \mid \sigma,A,I)$, via

$$P(f \mid d,\sigma,A,I) = \frac{P(d \mid f,\sigma,A,I)P(f \mid \sigma,A,I)}{P(d \mid \sigma,A,I)}. \tag{3}$$

Note that $P(f \mid \sigma,A,I) = P(f \mid I)$ due to the logical independence of f and σ respectively A. The terms "posterior" and "prior" have a logical, rather than a temporal, meaning. They simply express "with" and "without" respect to the new data. As the problem is formulated for given data, here the probability density $P(d \mid \sigma,A,I)$ is a normalization constant. The likelihood function $P(d \mid f,\sigma,A,I)$ reveals the error statistics of the experiment. In the present case of a counting experiment we are dealing with a Poisson function

$$P(d \mid f,\sigma,A,I) = \prod_{i=1}^{N_d} \frac{D_i^{d_i}}{d_i!}\mathrm{e}^{-D_i}, \tag{4}$$

where

$$D_i = \sum_{j=1}^{N_f} A_{ij} f_j. \tag{5}$$

The most uninformative prior $P(f \mid I)$ for a PAD is the entropic prior [18]

$$P(f \mid \alpha,I) = \frac{1}{Z}\mathrm{e}^{\alpha S}, \tag{6}$$

where

$$S = \sum_{j=1}^{N_f}\left(f_j - m_j - f_j \ln\left(\frac{f_j}{m_j}\right)\right). \tag{7}$$

The entropy S reveals the information divergence relative to the default model m_j. We use an uninformative flat default model, $m_j = c,\ 1 \leqslant j \leqslant N_f$, where c is given by maximizing

$$P(d \mid f,\sigma,A,I) = \prod_{i=1}^{N_d} \frac{D_i^{d_i}}{d_i!}\mathrm{e}^{-D_i}, \quad D_i = c \cdot \sum_{j=1}^{N_f} A_{ij}.$$

Z is a normalization constant. The width of $P(f \mid \alpha,I)$ is controlled by the regularization parameter α, that has to be marginalized $P(f \mid I) = \int \mathrm{d}\alpha P(f \mid \alpha,I)P(\alpha)$ with respect to a suitable prior $P(\alpha)$ [16]. As the entropic prior not fully suppresses insignificant oscillations within the deconvoluted spectra, a powerful technique for adaptively reducing the number of degrees of freedom (DOF) of a form-free reconstruction, the so-called adaptive kernel method, was developed [19]. The multi-resolution technique provides a local smoothness property with a high smoothness level in unstructured regions of the spectrum, and a low smoothness level where structures arise. Smoothness on f is imposed through a convolution of a hidden density h with a smoothing kernel B,

$$f(x;h,b) = \int \mathrm{d}y B\left(\frac{x-y}{b(y)}\right)h(y). \tag{8}$$

The local kernel width $b(y)$, which varies with y, and the shape of the kernel B are determined by

Bayesian methods. Details can be found in [14]. The numerical calculations of the reconstructing procedure do not exceed the experimental effort.

3.2. Apparatus function

Beside the measured spectra, it is the apparatus function $A(E', E - E')$, which provides essential information for the accuracy of the deconvolution. Therefore one has to attach greatest importance to the determination of the apparatus function $A(E', E - E')$ and its uncertainty. As a matter of principle the apparatus function $A(E', E - E')$ can be derived in two different ways: the experimental way via measuring a sample with known structure or via theoretical calculations of the different contributions to the energy broadening. Although both possibilities imply obvious uncertainties, we will demonstrate that they can be used to determine a reasonable upper and lower limit for the width of the apparatus function $A(E', E - E')$. Here, the procedure will be presented for $^{13}C^{5+}$ ions recoiled of a $^{13}C/^{12}C$ sample utilizing a 25 MeV ^{35}Cl beam, an incident angle of 7.5° and a scattering angle of 15°.

The experimental determination of $A(E', E - E')$ requires a suitable calibration sample. Here we will use the already mentioned $^{13}C/^{12}C$ multilayer sample (Fig. 4) that was thermally grown via electron beam evaporization of isotopically enriched ^{13}C (99 at.% ^{13}C, 1 at.% ^{12}C) and natural carbon, respectively. It consists of several ^{13}C layers about 0.1 μg/cm^2 thick, separated by ^{12}C layers about 1 μg/cm^2 thick. Supposing a box-shaped intrinsic depth profile (Fig. 5(a)), one will generate an apparatus function $A_{exp}(E', E - E')$ with a maximum width. This results due to the fact that the real intrinsic profile of the calibration sample is wider than the supposed box-shaped one. Therefore, the deconvolution with respect to this apparatus function $A_{exp}(E', E - E')$ reveals structures, whose widths represent a lower limit, if the surface roughness and inhomogeneity of the investigated sample do not exceed the surface roughness and inhomogeneity of the utilized calibration sample and if broadening due to data noise is neglected.

Knowing the intrinsic structure of a measured calibration sample the apparatus function $A_{exp}(E', E - E')$ can be generated via inversion of Eq. (2) using the adaptive kernel method, but with

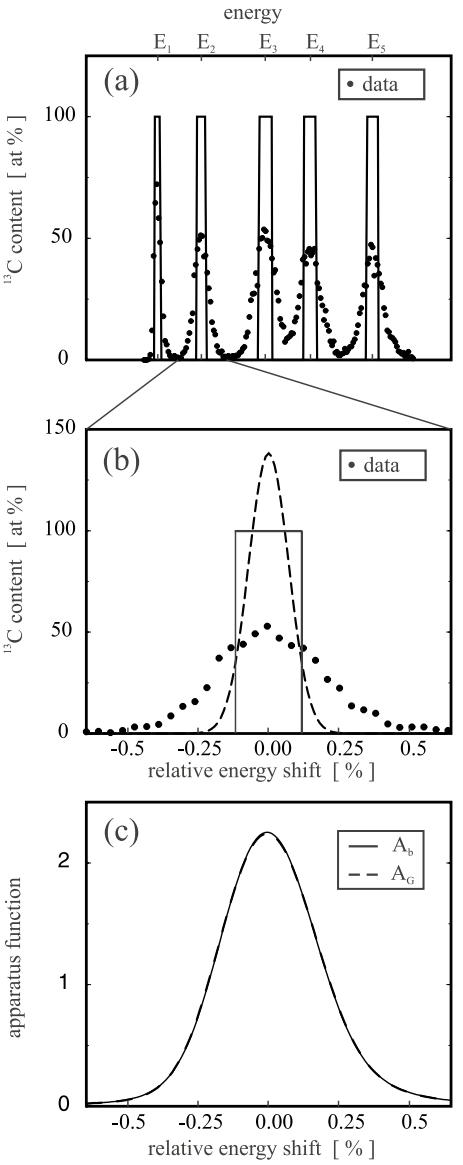

Fig. 5. Deconvolution of the apparatus function A with respect to a box-shaped and a Gaussian intrinsic profile of equal variance, respectively. Both deconvolutions (solid line: box-shaped intrinsic profile; dashed line: Gaussian intrinsic profile) are plotted in (c) and yield almost identical apparatus functions A_b and A_G.

the restriction to a certain energy E' and to clearly separate structures within the measured spectrum. In our case a deconvolution of the apparatus function $A_{\exp}(E', E - E')$ is possible for the energies $E' = E_1$, $E' = E_2$ and $E' = E_5$ (Fig. 5(a)). For $E' = E_2$, the deconvolution with regard to a box-shaped intrinsic profile on the one hand, and a Gaussian intrinsic profile on the other hand, with equal variance, respectively (Fig. 5(b)), yields almost identical Gauss-shaped apparatus functions $A_{\exp}(E_2, E - E_2)$ (Fig. 5(c)). For this reason and for the fact, that the dominating contributions to the energy broadening are Gauss-shaped, it is reasonable to generate the apparatus function $A_{\exp}(E', E - E')$ as follows:

The apparatus function $A_{\exp}(E', E - E')$ is assumed to be Gauss-shaped,

$$A(E', E - E') = \frac{1}{\sqrt{2\pi}\sigma_A(E')} \exp\left[-\frac{1}{2}\left(\frac{E - E'}{\sigma_A(E')}\right)^2\right]. \quad (9)$$

The peaks in the measured $^{13}C/^{12}C$ multilayer spectrum $\tilde{f}$ are fitted with Gaussian functions. The variance of the apparatus function $\sigma_A^2(E_i)$ is calculated by

$$\sigma_A^2(E_i) = \sigma_{\tilde{f}}^2(E_i) - \sigma_f^2(E_i), \quad 1 \leqslant i \leqslant 5, \quad (10)$$

where $\sigma_{\tilde{f}}^2(E_i)$ and $\sigma_f^2(E_i)$ are the variances of the fitted Gaussian functions and the box-shaped intrinsic spectrum, respectively. In order to provide an upper limit for the width of the apparatus function, a maximum error of 10% in the described procedure is considered. A polynomial fit through $(E_i, 1.1 \times \sigma_A(E_i))$ gives $\sigma_A(E')$, respectively $\sigma_A(x)$ within the entire energy respectively depth bin (Fig. 6(a)). The exhibited decrease of $\sigma_A(x)$ in depths $x > 2 \times 10^{17}$ at/cm^2 may be due to cumulating thickness fluctuations during growth of the $^{13}C/^{12}C$ multilayer sample.

In order to treat the theoretical approach the energy spreads were calculated using the DEPTH code of Szilágy et al. [20]. As this was done only with respect to the energy broadening induced by energy-loss straggling, multiple scattering and an intrinsic detector resolution $\Delta E/E = 2 \times 10^{-4}$, the derived energy spreads are considered as a lower

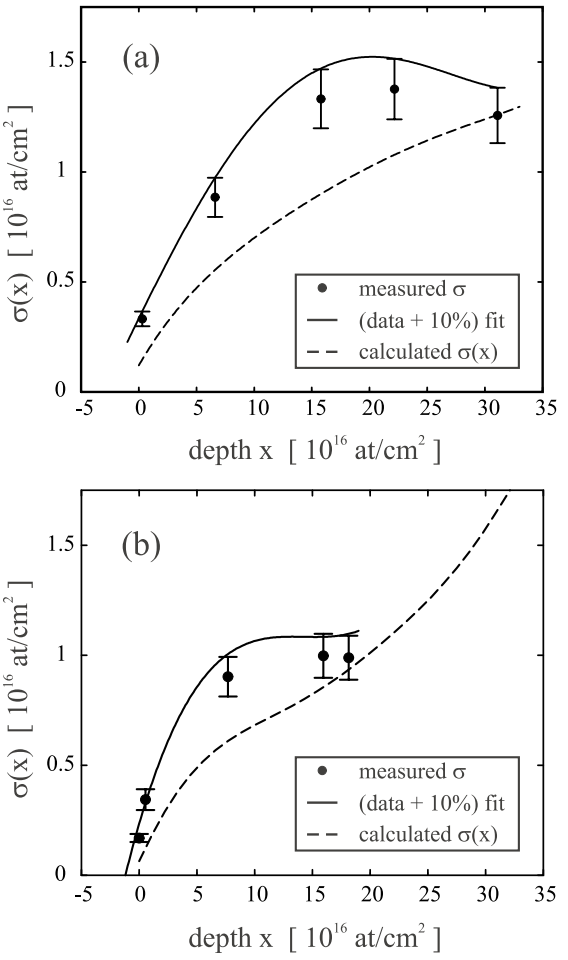

Fig. 6. Comparison of the standard deviations of the measured apparatus function with the corresponding calculated (DEPTH) values for (a) $^{13}C^{5+}$ ions recoiled of a carbon sample utilizing a 25 MeV ^{35}Cl beam, an incident angle of 7.5° and a scattering angle of 15° and (b) $^{13}C^{4+}$ ions recoiled of a carbon sample utilizing a 40 MeV ^{197}Au beam, an incident angle of 4° and a scattering angle of 15°.

limit for the variance σ_A^2 of the apparatus function A_{DEPTH}. Here it is in demand to discuss whether structures of maximum widths are obtained if the spectra are deconvoluted using the theoretical apparatus function A_{DEPTH}. A problem arises due to energy-loss straggling, which is calculated in DEPTH code according to Bohr's formula including corrections introduced by Chu et al. [20]. Earlier measurements for 60 MeV Ni ions revealed less energy-loss spread than the mentioned theories

[1]. As accurate measurements of the energy spread for the currently used ions are missing, the calculated values are not assured. In contrast to the calculated values the measured apparatus function A_{exp} includes broadening effects induced by specific sample properties such as mixed interfaces, surface roughness, density and thickness fluctuations of the carbon films in the samples as well as impurities, Therefore, the width of the measured apparatus function σ_{exp} must be larger than the calculated value σ_{DEPTH}. The fact that in Fig. 6(a) the measured and calculated widths of the apparatus function become almost equal in the depth $x = 3 \times 10^{17}$ at/cm^2 may also indicate that the DEPTH code is overestimating the energy spread due to energy-loss straggling or/and multiple scattering. Therefore, the width of a reconstruction using A_{DEPTH} can only be considered as an upper limit under reserve.

Fig. 6(b) exhibits the standard deviation of the measured apparatus function σ_{exp} and the calculated value σ_{DEPTH} for a 40 MeV ^{197}Au beam, an incident angle of 4° and a scattering angle of 15°, which are the utilized conditions in the experiment presented in Section 4. For the 40 MeV ^{197}Au beam, three values for the measured apparatus function $\sigma_{exp}(x)$ were determined as described above using the measured ^{13}C depth profile of the ^{13}C/^{12}C multilayer sample. The standard deviations $\sigma_{exp}(x = 0)$ and $\sigma_{exp}(x = 1.8 \times 10^{17}$ at/cm$^2)$ were derived by measuring the ^{13}C depth profile of an about 1.8×10^{17} at/cm^2 thick ^{13}C layer, that was thermally grown via electron-beam induced vaporization–condensation. Supposing a box-shaped intrinsic profile the rising slope from 13% to 87% of the maximum value within the measured spectrum reveals the depth resolution at the surface being the FWHM of the Gaussian apparatus function for depth $x = 0$. The analoguos procedure for the falling slope gives $\sigma_{exp}(x = 1.8 \times 10^{17}$ at/cm$^2)$.

To summarize the ingredients of the reconstructing procedure, we have to start with the Bayes theorem, assigning the likelihood probability from the error statistics of the experiment and the prior probability for a positive additive distribution. In addition, we use the adaptive kernel method in order to suppress insignificant oscillations within the reconstructed spectra. The apparatus function is determined via measuring a suitable calibration sample as well as via calculating the energy spreads using the DEPTH code of Szilágy et al. In order to consider the error due to the uncertainty of the apparatus function, the measured spectra are deconvoluted with regard to the measured and calculated apparatus function, respectively. As the deconvolution formalism using Bayes theorem inherently considers statistical errors, confidence intervals for the reconstructed spectra can be evaluated. The described procedure will be demonstrated in the subsequent section.

4. ^{13}C depth profiles in tetrahedral amorphous carbon (ta-C)

Some high-resolution ERD measurements of ta-C films will be shown in order to demonstrate the power of ERD analysis which is to quantitatively measure the depth profile of light elements in ultra-thin layers.

4.1. Properties of ta-C

In recent years there has been much interest to grow ta-C material. This material exhibits many extreme properties such as high hardness, high resistivity, optical transparency, chemical inertness, and a good thermal stability. Thin-film growth of ta-C is only possible with techniques involving energetic ions. Moreover, a characteristic ion-energy dependence of the phase formation is experimentally observed. In particular, the sp^3-bond fraction of ion deposited amorphous carbon (a-C) thin-films is exceeding 50% for ion energies between 50 eV and 1 keV. Below and above this energy range the amount of sp^2-bonded carbon atoms increases [21]. The ion-energy dependence on the evolution of diamond-like phases, above all the pronounced ion-energy dependence of the sp^3-bond fraction in a-C films, has been subject to a number of experimental and theoretical studies. However, the nucleation and growth mechanisms of ta-C, especially the strong influence of the ion energy have not been well understood [22].

4.2. Sample preparation

In order to provide experimental data for surveying and further improving existing models of thin-film growth of dense, diamond-like materials we have analyzed mean ion ranges and mixing zones involved in ion-beam deposition of ta-C using high-resolution ERD. The investigated samples were specially designed for this analysis and were deposited by mass-selected ion-beam deposition (MSIBD), a technique, which provides the purest deposition conditions [23]. Two different classes of ta-C films were grown: For the first class of films, initially about 12 nm ^{12}C were deposited onto sputter-cleaned Si (1 0 0) substrates with defined ion energy E_{ion}. In the subsequent step about 5×10^{14} at/cm^2 ^{13}C were deposited with the same E_{ion}. The second class of samples was grown as described above, but with the distinction that finally another 7 nm ^{12}C (this corresponds to about 1×10^{17} at/cm^2 ^{12}C) were deposited with the same E_{ion}. Using this procedure ta-C films were grown, that contain either directly on the surface or 7 nm beneath the surface about 5×10^{14} at/cm^2 ^{13}C. The small amount of 5×10^{14} at/cm^2 ^{13}C was chosen in order to assure that mixing effects by the ^{13}C incoming ions themselves during the deposition of the ^{13}C surface layer can be neglected. These samples are supposed to be ideal structures to measure ion ranges at very low energies using the films with the topmost ^{13}C layer and to investigate mixing zones obtained by ta-C growth using the films with the ^{13}C interfacial layer.

4.3. Experimental conditions

^{13}C depth profiles of films grown with deposition energies $E = 40$ eV and $E = 230$ eV were measured with 40 MeV ^{197}Au ions, an incident angle $\alpha = 4°$ and a scattering angle $\varphi = 15°$. The measurements were performed at a pressure of 1×10^{-8} mbar inside the scattering chamber of the Q3D magnetic spectrograph. It was proven by high-resolution ERD analysis that surface was only contaminated with about 2×10^{14} at/cm^2 oxygen, which do not significantly disturb depth profiles even in the range of monolayer resolution. Standard ERD measurements revealed a hydrogen content of about 2 at.% for the ta-C films. Other elemental concentration amounted to less than 10^{13} at/cm^2. The spectra are deconvoluted with respect to A_{exp} and A_{DEPTH} using the adaptive kernel method. The results of the analysis with respect to mean ion ranges and widths of the mixing zones will be discussed in detail in a subsequent publication. Here the power of the method in thin-film analysis will be demonstrated.

Irradiation-damage effects are investigated at first. Such investigations are routinely done during our measurements in order to get a knowledge of whether the measured profiles are reliable images of the depth profiles of the original sample or not. Utilizing the 40 MeV ^{197}Au beam no essential alteration of the ta-C samples was observed in the high-resolution measurements. Sputter processes, which limited the analysis utilizing 120 MeV ^{197}Au or 60 MeV ^{127}I ions in earlier measurements, are no longer a limit analysing the carbon samples.

4.4. Yield of 4+ charge state and point of zero thickness

The depth-dependent yield of the analyzed 4+ charge state of the ^{13}C recoil ions and the point of zero thickness have to be determined in order to get quantitative profiles. Both calibrations are done using a ta-C layer of pure ^{13}C that has been grown by depositing about 4×10^{16} at/cm^2 ^{13}C with kinetic energy $E_{\text{ion}} = 100$ eV. Fig. 7(a) shows the maximum-a-posteriori (MAP) solutions $\hat{f}_{\text{exp}}$ (with respect to A_{exp}) and $\hat{f}_{\text{DEPTH}}$ (with respect to A_{DEPTH}) for the ^{13}C depth profile of that sample. Both reconstructions as well as the data fit exhibit fluctuations of the profile with one shoulder at about zero thickness and two significant peaks and one dip up to a thickness of 1×10^{16} at/cm^2. The origin of that fluctuation is not yet clear. Charge–exchange processes in the non-equilibrium region are expected to reveal a smooth profile [24]. Oscillations in stopping power are not reported even if charge-state dependent non-equilibrium effects occur [25]. Surface-channeling effects should also not be relevant since the critical angles for channeling are more than one order of magnitude smaller than the ions incidence or exit angles. Therefore, the measured profile reveals a structure which represents a fluctuation of

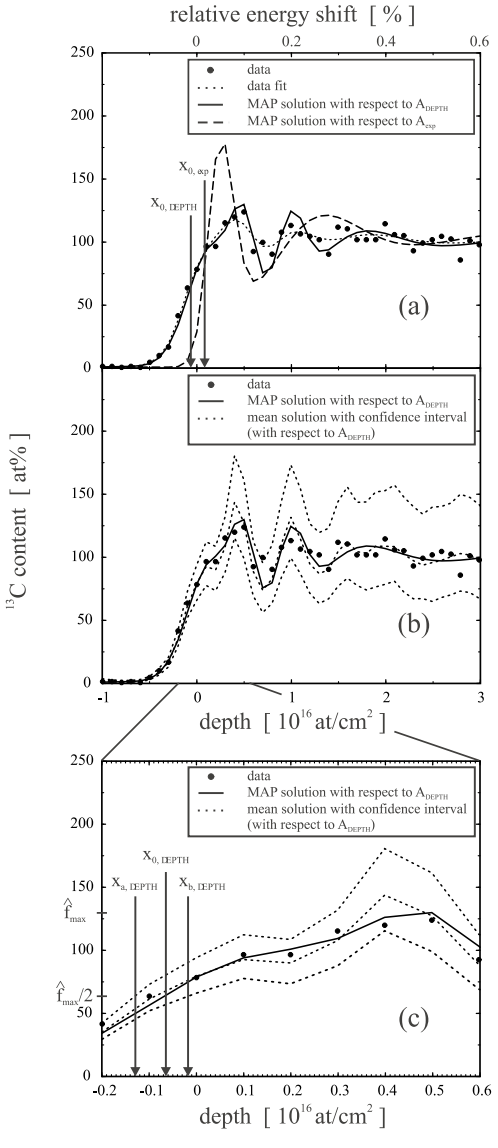

Fig. 7. ^{13}C spectrum of a ta-C sample that has been grown by depositing about 4×10^{16} at/cm^2 ^{13}C with kinetic energy $E_{\text{ion}} = 100$ eV. The MAP solutions with respect to A_{exp} and A_{DEPTH} are shown in (a). The MAP solution, the mean solution and the confidence interval with regard to A_{DEPTH}, respectively, are depicted in (b) (enlarged in (c)) as two presentations of the most important properties of the posterior probability density.

the ratio of electron and nuclear density on an atomic scale. It is similar to that which was measured for pyrolithic graphite where the structure of graphitic planes was resolved [1]. A clustering of carbon where the density oscillates with depth is possible although the samples do not show any long-range order from diffraction experiments.

With respect to the 4+ charge yield, the yield is constant neglecting the oscillations due to the assigned density fluctuations. Beam dose is calibrated using scattered silicon ions from the substrate detected by a standard $\Delta E - E_{\text{Res}}$ ERD detector [26] at scattering angle $\varphi = 40°$. A constant yield of 55% of ions with charge state $q = 4+$ is thereby assumed throughout the profiles.

The determination of the surface as the point of zero thickness within the measured spectra is a crucial point in order to get an accurate depth scale since energy scale is difficult to calibrate absolutely within the desired accuracy. Zero thickness is taken at the point where the rising ^{13}C spectra in Fig. 7(a) amounts 50% of the maximum value. The reconstructions with regard to A_{exp} and A_{DEPTH}, respectively, give two values $x_{0,\text{exp}}$ and $x_{0,\text{DEPTH}}$ with $x_{0,\text{exp}} - x_{0,\text{DEPTH}} \approx 1.6 \times 10^{15}$ at/cm^2. In order to quantify the error of these values, confidence intervals for each deconvolution have to be derived. This is done by Markov-Chain Monte Carlo (MCMC) integration [27]. For the calculated apparatus function A_{DEPTH}, a comparision of the MAP solution $\hat{f}_{\text{DEPTH}}$ and the mean solution $\langle f_{\text{DEPTH}} \rangle$ with the confidence interval $\sqrt{\langle (\Delta f_{\text{DEPTH}})^2 \rangle}$ is depicted in Fig. 7(b). The mean resolution and the MAP solution show an excellent match. Notice that the two solutions are only two different ways to represent the most important properties of the posterior probability density $P(f \mid d, \sigma, A, I)$. The confidence interval represents ± 1 standard deviation of the posterior probability density. Due to the depth dependence of the apparatus function the confidence interval is increasing with increasing depth. The two surface peaks are significant. Calculating the error of $x_{0,\text{DEPTH}}$, a lower and an upper limit for $x_{0,\text{DEPTH}}$ is given by the two values $x_{a,\text{DEPTH}}$ and $x_{b,\text{DEPTH}}$ where

$$\langle f(x_{(a,\text{DEPTH}),(b,\text{DEPTH})}) \rangle \pm \sqrt{\langle (\Delta f(x_{(a,\text{DEPTH}),(b,\text{DEPTH})}))^2 \rangle}$$

amounts to 50% of the maximum value of the MAP solution $\hat{f}_{\text{DEPTH}}$, respectively. Fig. 7(c) re-

veals $(x_{0,\mathrm{DEPTH}} - x_{a,\mathrm{DEPTH}}) \approx 0.7 \times 10^{15}$ at/cm^2 and $(x_{b,\mathrm{DEPTH}} - x_{0,\mathrm{DEPTH}}) \approx 0.5 \times 10^{15}$ at/cm^2. The analogous procedure with respect to A_{exp} gives $(x_{0,\mathrm{exp}} - x_{a,\mathrm{exp}}) \approx 0.4 \times 10^{15}$ at/cm^2 and $(x_{b,\mathrm{exp}} - x_{0,\mathrm{exp}}) \approx 0.5 \times 10^{15}$ at/cm^2. Thus, taking into account the respective errors of $x_{0,\mathrm{DEPTH}}$ and $x_{0,\mathrm{exp}}$, zero thickness $x_0 = (x_{a,\mathrm{DEPTH}} + x_{b,\mathrm{exp}})/2$ is quantified with an accuracy of $\pm 1.4 \times 10^{15}$ at/cm^2, which corresponds to ± 1.4 Å for a supposed density of 2 g/cm^3 near the surface.

4.5. Mixing and range of low-energy carbon ions

Fig. 8 shows the most probable solutions $\hat{f}_{\mathrm{exp}}$ and $\hat{f}_{\mathrm{DEPTH}}$ for the ^{13}C surface profiles of the ta-C samples, that have been deposited with energies $E = 40$ eV and $E = 230$ eV. For $E = 40$ eV, the reconstruction with respect to A_{exp} is much narrower than the reconstruction $\hat{f}_{\mathrm{DEPTH}}$ and the datafit (Fig. 8(a)). This is due to the fact that in depth $x \approx 5 \times 10^{15}$ at/cm^2 the width of A_{exp} is about 3 times larger than the width of A_{DEPTH} (Fig. 6) and that the width of the observed structure and the width of A_{exp} are of the same magnitude. The reconstructions in Figs. 8(a) and (b) reveal nonsymmetric structures, respectively, the rising slopes are steeper than the falling ones. With respect to the apparatus functions A_{exp} and A_{DEPTH}, the mean ion range $\bar{x} = \sum_{i=m}^{l}(x_i f_i)/\sum_{j=m}^{l} f_j$ and its error are calculated by a MCMC integration. Here, the starting and the stopping values x_m and x_l are chosen, so that $\langle f(x_m)\rangle$ amounts to 10% of the maximum value of $\langle f(x)\rangle$ within the rising slope of the spectrum and $\langle f(x_l)\rangle$ within the falling slope, respectively. Taking into account the respective results for both apparatus functions A_{exp} and A_{DEPTH} reveals a mean ion range of $(4.5 \pm 1.8) \times 10^{15}$ at/cm^2 for $E = 40$ eV and of $(12.6 \pm 2.0) \times 10^{15}$ at/cm^2 for $E = 230$ eV, whereas the dominating part of the derived error is attributed to the uncertainty of zero thickness.

The MAP solutions for the 40 eV interfacial profile shown in Fig. 9(a) are much wider than the respective reconstructions for the corresponding surface profile (Fig. 8(a)). This marks a mixing of the carbon during subplantation. Fig. 9(b) depicts the MAP solution $\hat{f}_{\mathrm{exp}}$, the respective mean solution $\langle f_{\mathrm{exp}}\rangle$ and its confidence intervals $\sqrt{\mathrm{var}(f_{\mathrm{exp}})}$

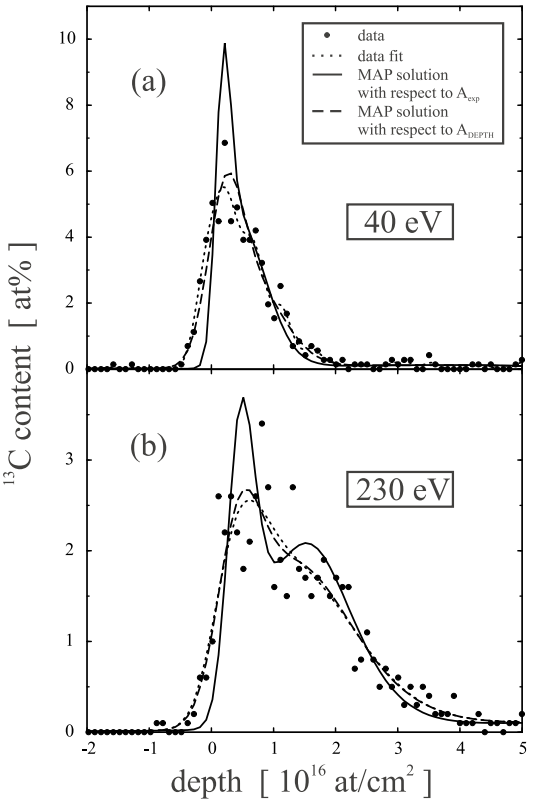

Fig. 8. MAP solutions of the measured surface profiles for the deposition energies $E = 40$ eV and $E = 230$ eV.

with regard to A_{exp}, respectively. The standard deviation of the mixing structure

$$\sqrt{\mathrm{var}(\mathrm{mix})} = \sqrt{\sum_{i=m}^{l}(x_i - \bar{x})^2 f_i \Big/ \sum_{j=m}^{l} f_j}$$

and its error are calculated via MCMC integration, where x_m and x_l are determined as described above. For the reconstructions with respect to A_{exp} and A_{DEPTH} the standard deviations

$$\sqrt{\mathrm{var}(\mathrm{mix})_{\mathrm{exp}}} = (10.9 \pm 0.5) \times 10^{15}\ \mathrm{at/cm^2}$$

and

$$\sqrt{\mathrm{var}(\mathrm{mix})_{\mathrm{DEPTH}}} = (13.1 \pm 0.4) \times 10^{15}\ \mathrm{at/cm^2}$$

were evaluated. The difference of the two values, which is much more than the respective errors, is

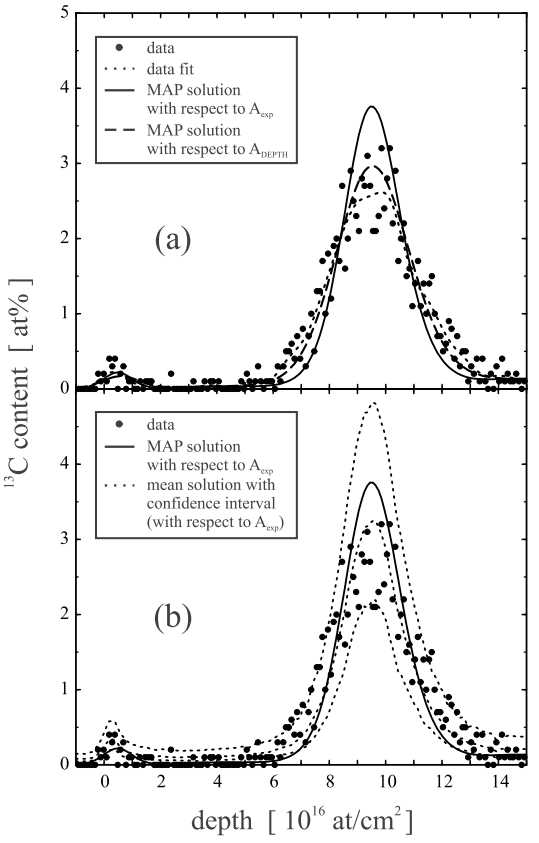

Fig. 9. Mixing profiles for the deposition energy $E = 40$ eV. The MAP solutions with respect to A_{exp} and A_{DEPTH} are shown in (a). With regard to the experimental apparatus function A_{exp}, a comparison of the MAP solution and the mean solution with confidence interval is depicted in (b).

due to the different number of channels that contribute to the summation. Therefore, a standard deviation of $(12.0 \pm 1.5 \times 10^{15})$ at/cm^2 is determined for the 40 eV mixing profile.

5. Conclusion

Depth resolution at the physical limit using large solid angles of detection is obtained in ERD measurements for the whole depth investigated, which is about 30 nm in carbon. Due to the improved angular resolution of the experimental setup all energy spreads induced by the large solid angle can be eliminated using the specific ion-optical arrangement of the Munich Q3D magnetic spectrograph and an additional numerical correction. A large solid angle (5 msr) in combination with heavy ion beams of about 0.2 A MeV enables us to measure elemental depth profiles for elemental contents below 1×10^{14} at/cm^2 without essentially altering the profiles during analysis. An apparatus function is determined and the depth resolution is improved by deconvoluting the measured spectra. It also allows to determine the uncertainty of the deconvoluted spectra and, for this reason, to quantify e.g. mixing widths and ion ranges of low-energy ions with respect to ta-C growth. Therefore, a wide field for quantitative investigations of light-elements depth distributions in ultra-thin films, at surfaces and at interfaces, is offered using the described technique.

Acknowledgements

This work is supported by the Tandem Accelerator Laboratory of the Technische Universität München and Ludwig-Maximilians-Universität München as well as by the Hahn Meitner Institut, Berlin. We want to thank Prof. V. Dose, Centre for Interdisciplinary Plasma Science, Max-Planck-Institut für Plasmaphysik, EURATOM Association, Garching, for careful proofreading.

References

[1] G. Dollinger, C.M. Frey, A. Bergmaier, T. Faestermann, Europhys. Lett. 42 (1998) 25.
[2] G. Dollinger, M. Boulouednine, A. Bergmaier, T. Faestermann, C.M. Frey, Nucl. Instr. and Meth. B 118 (1996) 291.
[3] M. Loeffler, H.J. Scheerer, H. Vonach, Nucl. Instr. and Meth. B 111 (1973) 1.
[4] G. Dollinger, Nucl. Instr. and Meth. B 79 (1993) 513.
[5] G. Dollinger, A. Bergmaier, T. Faestermann, C.M. Frey, Fresenius J. Anal. Chem. 353 (1995) 311.
[6] C. Albrecht, Diploma thesis, Technical University of Munich (unpublished).
[7] J.P. Stoquert, E. Guillaume, M. Hage-Ali, J. Grob, C. Ganter, P. Siffert, Nucl. Instr. and Meth. B 44 (1989) 184.
[8] A. Blažević, Ph.D. thesis, Freie Universität, Berlin, 1998.
[9] F. Pászti, E. Szilágy, E. Kótai, Nucl. Instr. and Meth. B 54 (1991) 507.

[10] G. Dollinger, T. Faestermann, P. Maier-Komor, Nucl. Instr. and Meth. B 64 (1992) 422.
[11] F. Seitz, J.S. Koehler, Solid State Phys. 2 (1956) 305.
[12] M. Toulemonde, E. Paumier, C. Dufour, Radiat. Eff. Def. Solids 126 (1993) 201.
[13] D. Lesueur, A. Dunlop, Radiat. Eff. Def. Solids 126 (1993) 163.
[14] R. Fischer, M. Mayer, W. von der Linden, V. Dose, Phys. Rev. E 55 (1997) 666.
[15] W. von der Linden, M. Donath, V. Dose, Phys. Rev. Lett. 71 (1993) 899.
[16] R. Fischer, Th. Fauster, W. von der Linden, V. Dose, Surf. Rev. Lett. 3 (1996) 1393.
[17] W. von der Linden, Appl. Phys. A 60 (1995) 155.
[18] J. Skilling, in: B. Buck, V. Macaulay (Eds.), Maximum Entropy in Action, Clarendon Press, Oxford, 1991, p. 19.
[19] R. Fischer, M. Mayer, W. von der Linden, V. Dose, Nucl. Instr. and Meth. B 136–138 (1998) 1140.
[20] E. Szilágy, F. Pászti, G. Amsel, Nucl. Instr. and Meth. B 100 (1995) 103.
[21] C. Ronning, E. Dreher, J. Thiele, P. Oelhafen, H. Hofsäss, Diam. Relat. Mater. 6 (1997) 830.
[22] H. Hofsäss, H. Feldermann, R. Merk, M. Sebastian, C. Ronning, Appl. Phys. Lett. 66 (1998) 513.
[23] H. Hofsäss, H. Binder, T. Klumpp, E. Recknagel, Diam. Relat. Mater. 3 (1994) 137.
[24] G. Dollinger, M. Boulouednine, A. Bergmaier, T. Faestermann, Nucl. Instr. and. Meth. B 138 (1998) 574.
[25] C.M. Frey, G. Dollinger, A. Bergmaier, T. Faestermann, P. Maier-Komor, Nucl. Instr. and. Meth. B 107 (1996) 31.
[26] A. Bergmaier, G. Dollinger, C.M. Frey, Nucl. Instr. and. Meth. B 136–138 (1998) 638.
[27] W.R. Gilks, S. Richardson, D.J. Spiegelhalter, Markov Chain Monte Carlo in Practice, Chapman & Hall, London, 1996.